Arab J Geosci
DOI 10.1007/s12517-013-0945-y

ORIGINAL PAPER

# Application of ASTER remote sensing data to geological mapping of basement domains in arid regions: a case study from the Central Anti-Atlas, Iguerda inlier, Morocco

**M'hamed El Janati · Abderrahmane Soulaimani · Hassan Admou · Nasrrddine Youbi · Ahmid Hafid · Kevin Patrick Hefferan**

Received: 5 January 2013 / Accepted: 1 April 2013


**Abstract** Satellite remote sensing is shown to provide critical support for geological and structural mapping in semiarid and arid areas. In this work, Advanced Spaceborne Thermal Emission and Reflection Radiometer (ASTER) data were used to clarify the geological framework of the Precambrian basement of the Iguerda Proterozoic inlier in the Moroccan Central Anti-Atlas. In this study, the interpretation of the processed digital data has been ground truthed with geological field data collected during a reconnaissance-mapping program in the Central Anti-Atlas. The Iguerda inlier offers a deeply eroded Precambrian massif dominated by a Paleoproterozoic basement composed of supracrustal metasedimentary units intruded by various Eburnian granitoids. Impressive mafic dyke swarms mainly of Proterozoic age crosscut this basement. Eburnian basement rocks are unconformably overlain by Lower Ediacaran volcanosedimentary rocks of the Ouarzazate Group and Upper Ediacaran–Lower Cambrian carbonates. The applied ASTER analyses are particularly effective in the lithological differentiation and discrimination of geological units of the Iguerda inlier. The spectral information divergence (SID) classification algorithm coupled with spectral angle mapper and maximum likelihood classification effectively discriminates between metamorphic rocks, granitoid bodies, and carbonate cover. SID classification improves geologic map accuracy with respect to the spatial distribution of plutonic bodies and metamorphic units. In addition, Paleoproterozoic granitoids have been well discriminated into separate distinct suites of porphyritic granites, granodiorites, and peraluminous leucogranite suites. This discrimination was initially identified via remote sensing analysis and later ground truthed in the field. This methodology enhances geological mapping and illustrates the potential of ASTER data to serve as a vital tool in detailed geologic mapping and exploration of well-exposed basement of arid regions, such as the Proterozoic of the Anti-Atlas Mountains of Morocco.

**Keywords** Anti-Atlas · Remote sensing · Geological mapping · ASTER data

M. El Janati · A. Soulaimani (✉) · H. Admou · N. Youbi
Department of Geology, Faculty of Sciences-Semlalia, Cadi Ayyad University, Prince Moulay Abdellah Avenue, P.O. Box 2390, Marrakech, Morocco
e-mail: soulaimani@uca.ma

A. Hafid
Department of Geology, Faculty of Sciences and Technics-Guéliz, Cadi Ayyad University, P.O. Box 549, Abdelkrim El Khattabi Avenue, Marrakech, Morocco

K. P. Hefferan
Department of Geography & Geology, University of Wisconsin-Stevens Point, 2001 Fourth Avenue,
Stevens Point, WI 54481, USA

## Introduction

Satellite remote sensing has become a common application in geological mapping and mineral discrimination. This technology is particularly useful in areas where conventional methods of geological mapping require large source time investment and high-risk fieldwork. Analysis of the spectral behavior of rocks using reflectance spectroscopy is therefore a valuable tool in remote sensing analysis that complements traditional field mapping methods.

Remote sensing analysis is widely used for geological and structural mapping in semiarid and arid areas. While significant results have been obtained for remote sensing of sedimentary domains (Lang 1999 and references therein),

Published online: 16 May 2013

enhanced imagery has been less effective in mapping metamorphic and igneous terrains. Recently however, interesting analytical results were obtained in crystalline basement using Advanced Spaceborne Thermal Emission and Reflection Radiometer (ASTER) and hyperspectral data (Rowan et al. 2011), in the Jbel Saghro at the eastern part of the Anti-Atlas (Massironi et al. 2008).

Multispectral remote sensing is an approach for enhancing digital thematic mapping by using training pixels (Schowengerdt 2007). Digital satellite images in the visible and infrared wavelength spectral range provide critical detail to the identification of lithological units and their spatial distribution. Advances in digital data and algorithm processing in remote sensing allow for advanced visualization and imagery interpretation.

The spectrometry imagery is particularly well received by geologist and cartographers, due to its sensitivity to physical and chemical properties, which allow identification of mineral assemblages in rock and soil (Chabrillat et al. 2000). Hyperspectral data are particularly useful due to their ability to achieve a very fine spatial resolution. Hyperspectral data contain at least ten spectral bands with relatively narrow spectral bandwidths extending continuously from visible to near infrared (VNIR) spectral regions (Baltsavia 2002).

During the last decade, ASTER multispectral imagery has offered improved spectral resolution and spatial detail compared to LANDSAT and has been shown to be effective in mapping earth surfaces. ASTER data provide improvements in the quality and quantity of information that can be gathered about geological survey and mapping due to the number of spectral bands and high resolution. ASTER imagery can be used to facilitate efficient field mapping.

Our study tests various processing algorithms based on spectral cluster statistics of ASTER images. This study examines the spatial accuracy pattern of thematic maps using several classification algorithms as applied to the geology of the Iguerda inlier in the Central Anti-Atlas Mountains of Morocco.

The Anti-Atlas belt is an arid, mountainous area of Morocco, south of the High Atlas range. It is largely devoid of soil and vegetation and is used here as a case study for testing remote sensing techniques to improve rock discrimination in the geologic mapping of a basement massif.

The Iguerda Proterozoic inlier has been the subject of a recent reconnaissance field mapping and prospecting program (Agadir Melloul Project 19/2008), part of the National Program of Geological Mapping (PNCG) launched by the Moroccan Ministry of Energy and Mines. The 1/50,000 scale geological maps generated during this project, in which the present authors participated as field geologists (Admou et al. 2013; Hafid et al. 2013; Chèvremont et al. 2013; Ouanaimi et al. 2003), provide ground truth data to test the spectral imagery results.

## Geological framework

### General geology of the Anti-Atlas

The Anti-Atlas belt (Fig. 1) corresponds to a broad ENE–WSW trending anticlinorium some 800 km long and 200 km wide, extending south of the High Atlas chain and north of the West African Craton (WAC) (Choubert 1963). Most of the Anti-Atlas basement was assembled during the final stage of the Eburnian orogeny at ca. 2 Ga (Rocci et al. 1991) forming the WAC itself. The Anti-Atlas region was subsequently affected by the Neoproterozoic Pan-African Orogeny and the Variscan thick-skinned tectonics (Soulaimani 1998; Caritg et al. 2004; Soulaimani and Burkhard 2008; Michard et al. 2011). Variscan orogeny has been responsible for the exhumation of Precambrian antiformal massifs, which have been exposed at the surface during the Jurassic–Early Cretaceous erosional interval (Ruiz et al. 2011) and now crop out in discrete inliers or "boutonnières" (Choubert 1943, 1963).

Precambrian basement rocks encompass several metamorphic and magmatic units of Paleoproterozoic to Neoproterozoic ages, unconformably overlain by Upper Ediacaran–Cambrian rocks, followed by thick sedimentary Paleozoic units. Two main Proterozoic tectono-magmatic events have been recognized in the Anti-Atlas: (a) At ca. 2 Ga, granitoid bodies and intruded metasedimentary and metavolcanic rocks are transformed during the Eburnian orogeny producing Paleoproterozoic gneisses and migmatites that outcrop exclusively southwest of the Anti-Atlas Major Fault (Choubert 1947). These rocks correspond to the Eburnian basement of the Anti-Atlas (Aït Malek et al. 1998; Walsh et al. 2002; Thomas et al. 2002; Gasquet et al. 2005). A long quiescence interval followed during Mesoproterozoic times, only interrupted by dyke emplacement at ~1,700 Ma (Gasquet et al. 2004) and 1,350 Ma (El Bahat et al. 2013); (b) In Neoproterozoic time, the Pan-African cycle (900–550 Ma) documents the breakup of the northern margin of the (WAC) and the onset of oceanic domain and volcanic arc development, followed by complex transpressive collage processes (Leblanc 1976; Leblanc and Moussine-Pouchkine 1994; Saquaque et al. 1989; Thomas et al. 2004; Gasquet et al. 2008). Indeed, in the Central Anti-Atlas region, Neoproterozoic siliciclastic-dominated platform units (Taghdout-Lkest Group) (Hassenforder 1987; Bouougri and Porada 2002), arc-related volcanosedimentary rocks (Thomas et al. 2002), and remnants of Neoproterozoic oceanic crust (Bou Azzer Group) (Saquaque et al. 1989; Admou and Juteau 1998) were assembled. All these units were deformed and accreted to the northern edge of the WAC as tectonic slices along the Bou Azzer–Siroua suture (Saquaque et al. 1989; Hefferan et al. 2000; Thomas et al. 2002) during two main Pan-African events at 760 and 650 Ma (D'Lemos et al. 2006; Inglis et al. 2005; Walsh et al. 2012). Above, Tiddiline and

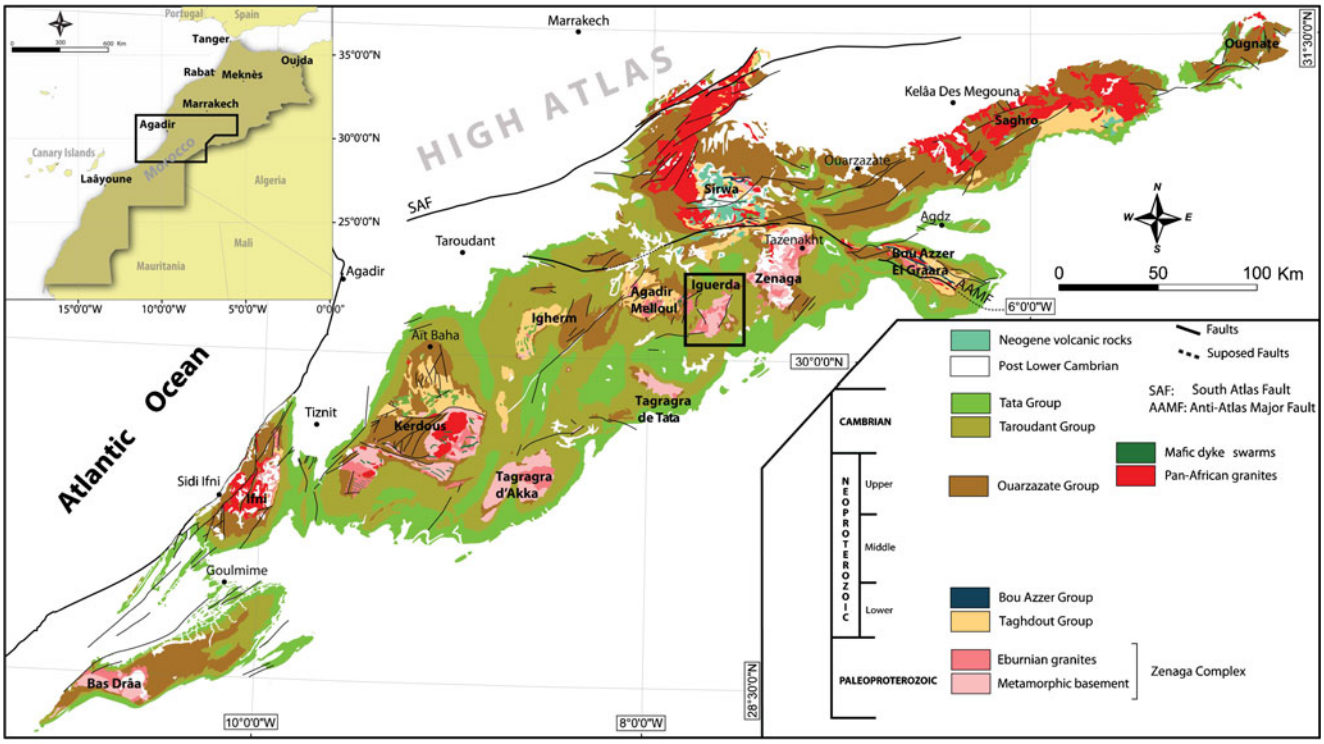


**Fig. 1** Location of the Iguerda inlier in the geological map of the Anti-Atlas (drawn from the geological map of Morocco 1/1,000,000)

Bou Salda Groups unconformably overlie these assemblages and were only affected by late stages of the Pan-African shortening (Hefferan et al. 1992; Thomas et al. 2002; El Hadi et al. 2010).

All these Proterozoic rocks are unconformably covered by the post-Pan-African continental volcanoclastic series of Ouarzazate Group and overlain by transgressive Paleozoic passive margin sedimentary sequence ~6- to 10-km thick, ranging from the Cambrian to Lower Carboniferous and outcropping mainly to the south of the Anti-Atlas.

During Late Carboniferous, basement fractures of the Anti-Atlas were remobilized and Precambrian blocks were compressed and affected by low-grade metamorphic conditions, inducing uneven folding in the overlying Paleozoic cover. At this time, the Anti-Atlas constituted the southern foreland area of the Alleghanian–Variscan belt (Soulaimani 1998; Burkhard et al. 2006; Soulaimani and Burkhard 2008).

Lastly, numerous Triassic–Liassic dykes and sills of the Central Atlantic Magmatic Provinces (CAMP) crosscut the Precambrian basement and Variscan folds of the Anti-Atlas (Youbi et al. 2003). Mesozoic deposits are not preserved on the mountain belt, except very locally (Cretaceous relicts on top of the Ifni and Siroua inliers). After burial during Cretaceous–Eocene times, the Anti-Atlas experienced its final exhumation during the Neogene, contemporaneously with the High Atlas itself (Ruiz et al. 2011).

## Geology of Iguerda inlier

The Iguerda inlier, the subject area of this work (Fig. 2), is located in the central part of Anti-Atlas between the Agadir Melloul inlier to the west and Zenaga to the NE. Due to limited accessibility, little work has been devoted to the Iguerda inlier such that this study provides new significant petrographic, geochronologic, and geodynamic data. The Iguerda inlier corresponds to a large NE–SW depression (15 km$^2$) 30 km long and 10 km wide, surrounded by 1,900-m-high Cambrian plateaus. Unlike other inliers of the Anti-Atlas, where bedrock usually forms large flat expanses, the Iguerda inlier contains highly variable relief due to highly variable rock types exhibiting differential weathering characteristics, numerous multidirectional mafic ridge-forming dyke swarms, and possibly differential vertical movements during the Cenozoic Alpine uplift (Ruiz et al. 2011).

The Iguerda inlier consists of metasedimentary country rocks, crosscutting Paleoproterozoic granitoids (historically referred to as "PI") and associated contact metamorphic aureoles (Agard 1954; Bilal and Derre 1989). Metasedimentary country rocks are derived from sandstone–pelitic sediments sourced from erosion of older undetermined basement. During Eburnian orogeny, this protolithe experienced variable greenschist to amphibolite regional metamorphism which is locally superimposed by a local thermal metamorphism. Micaschists are locally anatectic and intruded by granites, granite pegmatites, and associated migmatites

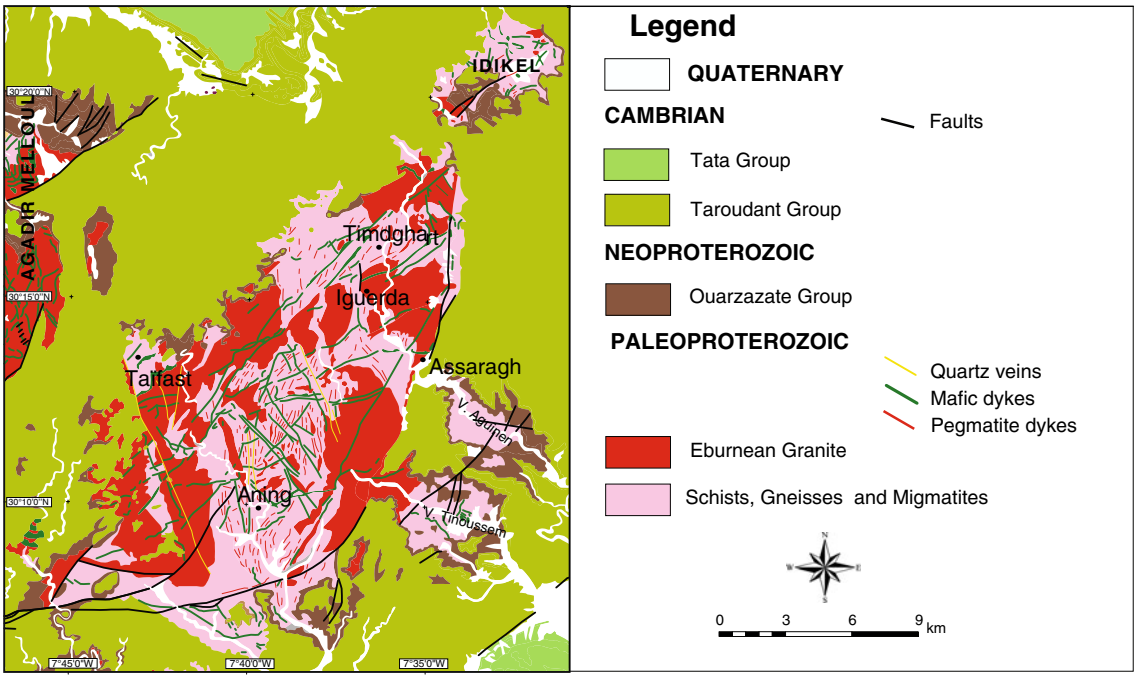


**Fig. 2** Geological map of Iguerda inlier (from Faure-Muret et al. 1992)

(Fig. 3a). The precise ages of the metamorphic events are poorly constrained within Iguerda inlier. However, SW of Iguerda, in the Tagragra of Tata inlier, metasediments have been directly dated at 2,072±8 Ma (Walsh et al. 2002). Further to the west in the Kerdous inlier, similar micaschists are crosscut by intrusions dated at 2,110±17 Ma (Roger et al. 2006) and 2,187±33 Ma (O'Connor et al. 2010).

Radiometric U-Pb SHRIMP zircon dates from Iguerda granitoids confirm their Paleoproterozoic age, ranging between 2,038 and 2,034 Ma (Admou et al. 2013; Chèvremont et al. 2013). Paleoproterozoic granitoids of Iguerda are divided into two magmatic suites: (a) a calc–alkaline medium potassic suite, composed of quartz monzodiorite, orbicular diorite, quartz diorite–tonalite, and mesocratic to subleucocratic porphyritic granites, and (b) a potassium aluminum suite which comprise mainly sub-leucocratic to leucocratic granites (Fig. 3b). The term "suite" herein used follows the lithodemic nomenclature of the North American Stratigraphic Code. Suites comprise two or more lithodemes, as they are lithodemic units next higher in rank to lithodemes. Lithodemes are bodies of predominantly intrusive, highly deformed, and/or metamorphosed rocks. Lithodemes generally are non-tabular, lack primary depositional structures, and are characterized by lithic homogeneity (North American Stratigraphic Code 2005). The first suite is derived from the differentiation of a mantle-derived magma, probably associated with a former Eburnian arc, while the second suite reflects the melting of supracrustal materials in a collisional environment. These two magma suites are well documented in other inliers of the Anti-Atlas (Mortaji et al. 2000; Thomas et al. 2002; Gasquet et al. 2004; Roger et al. 2006). These Paleoproterozoic granitic intrusions produced contact metamorphic aureoles, resulting in the growth of andalusite and/or cordierite blasts, particularly well developed around the large intrusive bodies.

The Paleoproterozoic basement of Iguerda area is crosscut by impressive mafic dyke swarm, some of which exceed several kilometers in length (Fig. 3c). Mainly of doleritic to microgabbroic nature, their trends occur in two major families: NW–SE and NE–SW. Most of the basic dykes have continental tholeiitic geochemical similarities (Hafid et al. 1998, 1999); El Aouli et al. 2001, 2004, 2010). However, several discrete pulses of dyke emplacement extend from the Paleoproterozoic to the Mesozoic. We can distinguish: (a) Paleoproterozoic veins similar to those dated in the inliers of Tagragra of Tata (Walsh et al. 2002) and Taznakht (Kouyaté et al. 2013); (b) Mesoproterozoic dykes (1.65 Ga) in the Agadir Melloul inlier (Kouyaté et al. 2013) and further west in the Tagragra of Akka (Gasquet et al. 2004); (c) Lower Neoproterozoic dykes of Ifzwane suite (Thomas et al. 2002) have been dated at 885 Ma (historically referred to as the beginning of "PII" events) in the Iguerda inlier (Kouyaté et al. 2013); (d) Ediacaran rifting dykes intrude the Ouarzazate Group; and finally (e), CAMP province dykes which crosscut the Cambrian cover are associated with the Triassic–Liassic opening of the Central Atlantic (Youbi et al. 2003).

The Paleoproterozoic basement of Iguerda inlier is unconformably overlain by rhyolite and volcanoclastic

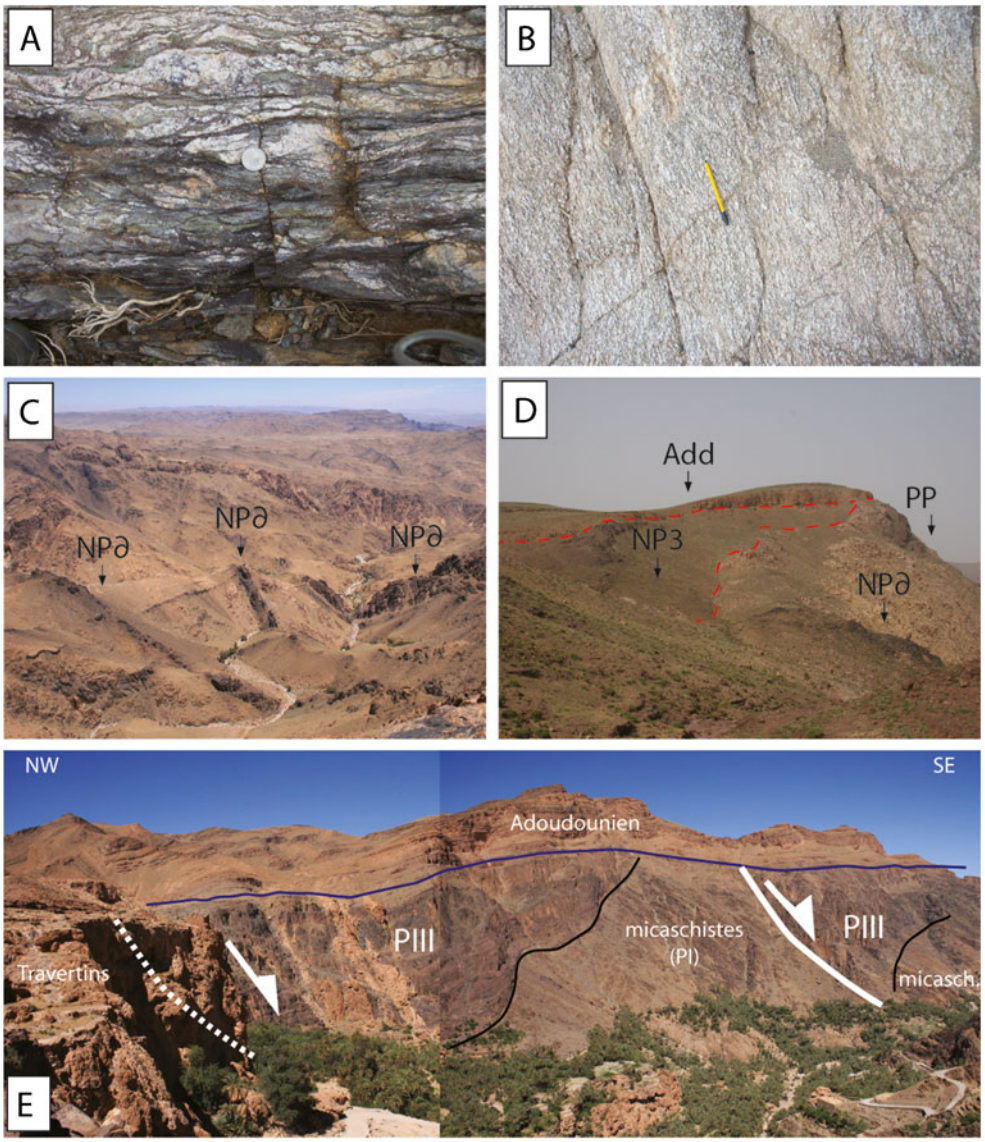


**Fig. 3** **a** Metasedimentary country rock of Iguerda inlier consisting of mica schist, locally anatectic. **b** Photograph of Paleoproterozoic granite. **c** Eastward view of the western part of Iguerda inlier showing the importance of mafic dyke swarms (*NPə*) crosscutting the Paleoproterozoic basement. **d** Volcanoclastic series of Ouarzazate Group (*NP3*) unconformably overlying the Paleoproterozoic granite (*PP*) at the western entrance of the inlier. The Adoudou Group limestones (*Add*) are transgressive over all of the Precambrian series. **e** E–W cross section along the northern side of the Aguinane Valley showing basement blocks tilted during the Ouarzazate Group rifting (*PIII*) which occur before the transgressive Adoudou Group limestones were deposited

rocks attributed to the Lower Ediacaran Ouarzazate Group (historically referred to as "PIII") (Fig. 3d). The Ouarzazate Group outcrops exclusively along the perimeter of the inlier and is deposited in tilted blocks of a Neoproterozoic–Cambrian rift system (Piqué et al. 1999, Soulaimani et al. 2003). The Ouarzazate Group is conformably or disconformably overlain (Fig. 3e) by the Upper Ediacaran–Lower Cambrian carbonate deposits (Taroudant and Tata Groups, respectively). During the Variscan orogeny, basement fractures of the Iguerda inlier were reactivated and the entire massif has been uplifted, inducing upright folds in the Adoudou Group limestones above remobilized faults.

## ASTER preprocessing and classification process

Preprocessing is an essential procedure to acquire spatially and radiometrically corrected images in order to analyze and interpret spectral data. Digital images require the application of different types of systematic corrections. Errors can be generated from the raw data or from noise corrections, effects of geometric distortion, and radiometric calibration (Liu and Mason 2009).

Preprocessing used in this study includes:

- Geometric corrections applied by transformation of the image into standard system coordinate through rectification. The rectified ASTER image is in a curved irregular shape indicating nonlinear distortion of the image in the reference map projection.
- Calibration of reflectance data was achieved by internal average relative (IAR) reflectance algorithm for each band of ASTER data. IAR reflectance correction has been used with considerable success in arid regions (Kruse 1988; Ben-Dor et al. 1994). IAR reflectance is calculated by determining an average spectrum for an

entire imaging spectrometer data set and dividing each spectrum in the data set by the average spectrum. The resulting spectra represent reflectance relative to the average spectrum and resemble laboratory spectra acquired from the same materials (Kruse 1988).

- The result can be used afterwards for selective enhancement and effective target discrimination. This last point may not cover all aspects of image processing, but obtained results constitute a useful guide to enhance a workable processing strategy, depending on the nature of the application.
- The specific area of interest was extracted in a subscene by deleting redundant parts using minimum noise fraction transform (MNF) algorithm to reduce spectral and spatial complexity of the data. The MNF processing reduces the spectral dimensionality of data by locating linear combinations of bands that match the inherent dimensionality of the data.
- Spectral image enhancement was utilized for advanced visualization and mapping and for testing different algorithms. This computational method, coupled with purity pixel index (PPI) and spatial spectral endmember extraction, can be used for classification and for the subsequent computational processing. PPI reduces the spatial dimensionality by finding key endmembers. Once endmember spectra are determined, automated identification procedures match endmember results with a spectral library. These identified image endmembers are applied to the full spatial dataset to create image maps showing the location and abundance of specific materials.

## ASTER data

The ASTER instrument has been built in Japan by a consortium of government, industry, and research groups. Every image obtained is in a gray scale from black to white based on the brightness of radiation at a precise wavelength (between 0.52 and 11.65 μm) (Table 1). ASTER data include radiation reflected in the VNIR spectral range. Three recording channels occur at wavelengths between 0.52 and 0.86 μm, with a spatial resolution of 15 m. Band "B3" is divided to B3b and B3n, using algorithms developed by an ASTER scientist team to generate a digital elevation model. The shortwave length infrared (SWIR) has six recording channels at wavelength between 1.6 and 2.43 μm, with a spatial resolution of 30 m. The thermal infrared subsystem (TIR) has five recording channels, with wavelengths between 8.125 and 11.65 μm and with a spatial resolution of 90 m.

VNIR wavelengths have been used widely for mineralization mapping (Knipling 1970) due to sensitivity to the presence of iron oxide minerals (Hunt 1979; Rowan et al. 1977). This FeO sensitivity helps in the study of sulfide ore deposits, such as gossans, massive sulfide, and hydrothermal deposits from Australia and Saudi Arabia (Raines et al. 1985). The near infrared wavelengths have been employed in classification mapping of regolith groups in Yilgarn Craton of Australia (McPherson and Halls 2007; Townsend 1987).

SWIR spectral ranges allow for discrimination of clays, phyllosilicates, alunite, and limestone (Hunt 1979). SWIR are useful for mapping chlorite-metamorphic alteration halos and white mica associated with porphyry hydrothermal Cu–Au mineralization (Marsh and McKeon 1983; Rowan et al. 1991). TIR data are sensitive to the abundance of silica and have been used in discriminating albitic granites in the Central Eastern Desert of Egypt (Aboelkhair et al. 2010).

## ASTER data processing

In this study, ASTER digital image processing has been applied to raw data. Processing data from multidimensional space to multispectral data is widely used for thematic extraction to produce very detailed mineral and lithological maps. While image processing can never increase the performance provided by the raw data, the use of appropriate image processing can improve visualization comprehension and analysis of the image information. The interpretation of the processed digital data has been ground truthed with geological field data collected during the reconnaissance-mapping program in the Iguerda area.

In this paper, several remote sensing approaches are used, including algorithms to: (a) convert the raw data to appropriate reflectance forms and select varied targets matched to enhance information visualization using the IAR reflectance algorithm (the internal average reflectance). IAR reflectance algorithm has been used with considerable success in arid regions (Ben-Dor and Kruse 1994). IAR algorithm determines an average spectrum for an entire image and divides each spectrum in the data set by the average spectrum; (b) Spectral endmember extraction and labeling of sample training targets define an efficient sampling selection and establish algorithms for the most informative training samples, thus optimizing assessment accuracy when coupled with ground truth knowledge. Other technical processing includes "minimum noise fraction method" (MNF) methods, PPI, and endmember selection, which allow us to select pure pixels in the scene as the first endmember.

## Minimum noise fraction method

Adapted by Green et al. (1988), MNF method is applied to our data in order to obtain reasonable segregation of coherent signals while reducing noise. MNF transform reduces the spectral dimensionality of data by locating linear combinations of bands that match the inherent dimensionality of the data

**Table 1** Wavelength and spatial range of ASTER data (Abrams 2000; Yamaguchi et al. 1998)

| Subsystems | | VNIR | | SWIR | | TIR |
|---|---|---|---|---|---|---|
| | B1 | 0.52–0.60 | B4 | 1.6–1.7 | B10 | 8.125–8.475 |
| | | Nadir looking | | | | |
| | B2 | 0.63–0.69 | B5 | 2.145–2.185 | B11 | 8.475–8.825 |
| | | Nadir looking | | | | |
| | B3n | 0.76–0.86 | B6 | 2.185–2.225 | B12 | 8.925–9.275 |
| Bands | | Nadir looking | | | | |
| | B3b | 0.76–0.86 | B7 | 2.235–2.285 | B13 | 10.25–10.95 |
| Spectral range (μm) | | Nadir looking | | | | |
| | | | B8 | 2.295–2.365 | B14 | 10.95–11.65 |
| | | | B9 | 2.36–2.43 | | |
| Spatial Resolution (m) | 15 | | 30 | | 90 | |
| Signal Quantization (bits) | 8 | | 8 | | 12 | |

*ASTER* Advanced Spaceborne Thermal Emission and Reflection Radiometer, *VNIR* visible and near infrared, *SWIR* shortwave infrared, *TIR* thermal infrared

(Fig. 4). This two-part process involves component correlation which maximizes variance between noise and spectral signature. The second part involves standard transformation to principal components, which creates 14 MNF bands, called "eigen-images."

Results (Fig. 3) show that the first set of MNF bands (B1 to B4) contains the most spectral information. Conversely, bands (B5 to B14) provide the minimum information, which allow us to reduce dimensionality and increase signal-to-noise ratio in bands with less spectral resolution.

## Purity pixel index and endmember extraction

Spectral endmember extractions are highly dependent on automatic or semiautomatic processing used to generate reasonable separation of spectral data. The PPI procedure (Boardman et al. 1995) permits an endmember identification for high-dimensional images. Likewise, it targets pure pixels while reducing space. Thus, PPI process, created from 14 eigen-images, reduces the number of pixels to be analyzed from the 14 MNF eigen-images. Each pixel value corresponds to a pure spectral pixel. A final number of classes are chosen from pixel combinations in conjunction with *n*-dimensional scatter, which we can use in any transformed space.

The visual review of pure pixels selected in *n*-dimensional scatter plot is conducted for all appropriate eigen-images. This automatic identification procedure is useful for the analysis of spectral data (Rogge et al. 2007). These spectral data components are used in *n*-dimensional

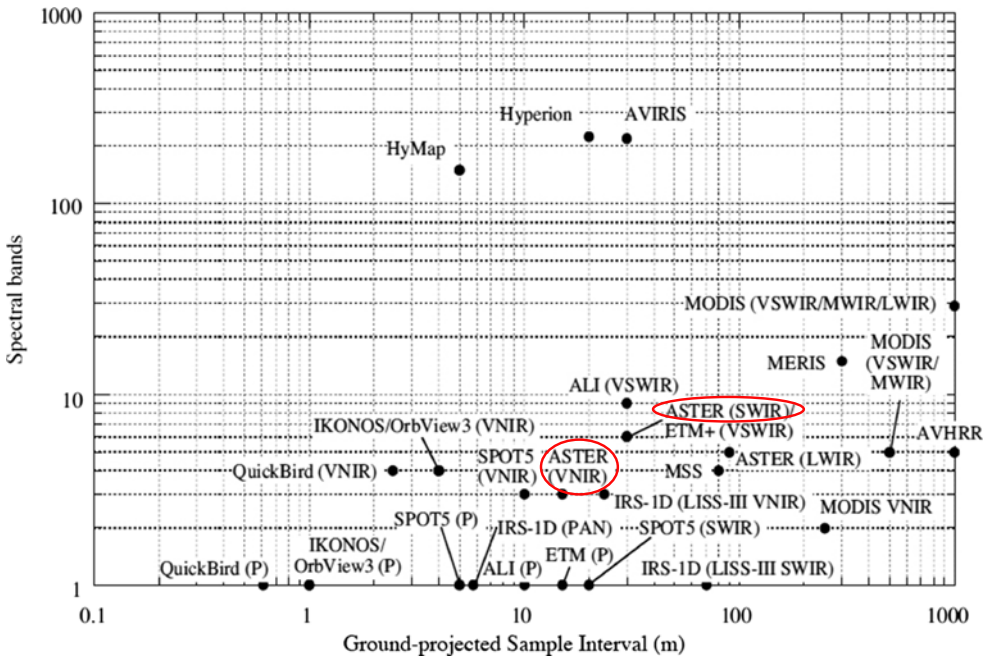


**Fig. 4** MNF eigenvalues plot with 14 MNF bands

scatter plots ($n$=number of bands) and displayed as distinct spectral endmembers.

In order to discriminate lithologic units constituting the Proterozoic basement of Iguerda inlier, 11 main classes of spectral components have been identified (Fig. 5) using the PPI algorithms, including: porphyritic granites, granodiorites, peraluminous leucogranites, micaschists, migmatites, mafic rocks, metasediments, massive rhyolite, volcanoclastic sediments, carbonates, and travertines.

In general, the global trends of these spectral signatures allow for effective discrimination of rock classes based on reflectance magnitude and angle distributed within 14 bands. These spectral components are extracted by $n$-dimensional visualization and then used as reference spectres for advanced visualization and mapping using the following classification algorithms.

## Classification algorithms, processing, and lithological mapping of Iguerda Proterozoic basement

In order to reduce the number of redundant pixels, each pixel is assigned to a predefined pixel class based on spectral components and statistical data of each class target. Classification algorithms distribute each pixel to the class target which contains the most similar characteristics.

Consequently, the process was automatically optimized according to cluster statistics suited to images of targets. Even for a well-mapped area, this may provide more accuracy by using spectral features. The results of thematic classifications are dependent upon algorithm classifications such as spectral angle mapper (SAM), spectral information divergence (SID), and maximum likelihood.

### Spectral angle mapper

Spectral angle mapper is a supervised classification algorithm based on statistical techniques and is dependent on the cluster identification of the image. This method computes spectral similarity between different spectral angles and their corresponding vectors (Yuhas et al. 1992; Kruse et al. 1993). The classification is carried out by minimizing the angle between a target and ideal position of the class in space.

The spectral distance is independent of the magnitude of spectral vectors, and therefore, this classification is insensitive to topography variations (De Carvalho and Meneses 2000). In this section, the SAM procedure is tested using ASTER data set, including varied lithological classes outcropping in the study area (Fig. 6a). Table 2 shows the results of SAM, which effectively discriminate porphyritic granites and metasediments. The threshold of levels mapped is generally used to empirically determine the regions corresponding to reference spectrum range, while maintaining their spatial coherence. Although SAM is limited to a partial screening of ASTER data, these algorithms are coupled to classification results of SID and maximum likelihood classification (MLC).

### Spectral information divergence

In order to refine classification of information already obtained with SAM, SID is applied to improve the accuracy of the estimate of endmember abundance used in optimal classification (Xu and Zhao 2008). The fraction of spectral components image resulting from this procedure displays a perfect correlation between the different lithological classes. In fact, SID appears most successful in distinguishing between major geological units. Good agreement is found between different classes derived by image quantification, which demonstrates the effectiveness of spectral components (Fig. 6b). In all instances, the current SID image provides consistent results (Table 2) for mapping granodiorite suites and shows correlation percentage at 93 %, peraluminous leucogranites at 99 %, and carbonate sediments at 81.29 %. The results of granite distribution indicate the closest match, and SID procedure provides the most detail of this survey.

### Maximum likelihood classification

The MLC is based on the probability that a pixel with the maximum likelihood, determined by measuring mean spectral vectors involved in the signature file, is classified into the corresponding class (Richards et al. 2006; Richards 1993; Jia et al. 1994). The extraction of common information is executed for the pure spectral components derived from reflectance spectral selection (Chen and Landgrebe 1989; Henderson et al. 1992). The classes are selected from ASTER bands to effect simple separation of lithological classes. Each class relates to a pure endmember pixel. The results are based on the accuracy of this classification and the available spectral components (Fig. 5). Ultimately, only a few classes were considered at this stage (Fig. 6c).

### Summary of algorithm results

In this study, SID is most successful in distinguishing between major geological units, particularly in the discrimination of granodiorites (93 % accuracy), peraluminous leucogranites (99 % accuracy), and carbonate sediments (81.29 % accuracy). Utilizing SAM and SID, intrusive granitoids are clearly identified and subdivided into three categories, which, ground truthed by our field observations, correspond to: (a) porphyritic granites; (b) granodiorites, and (c) peraluminous leucogranites. Previously, these three bodies were mapped as

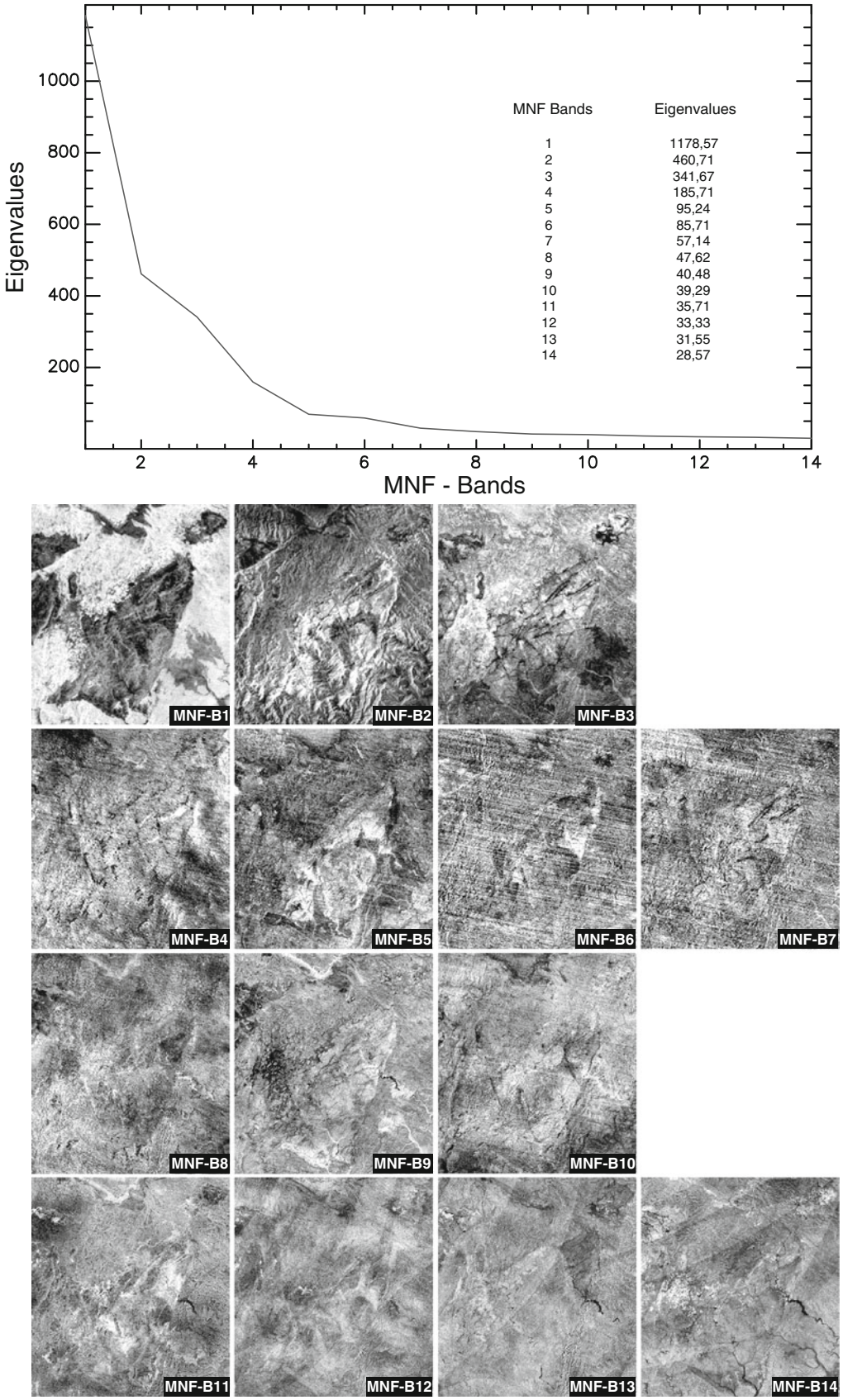


**Fig. 5** **a**–**c** Endmember reflection spectral features: (*1*) metasediments; (*2*) migmatites; (*3*) porphyritic granite suite; (*4*) micashists; (*5*) mafic rocks; (6) volcanoclastic sediment; (*7*) carbonates; (*8*) granodiorite suite; (*9*) massive rhyolitic; (*10*) peraluminous leucogranites; and (*11*) travertine

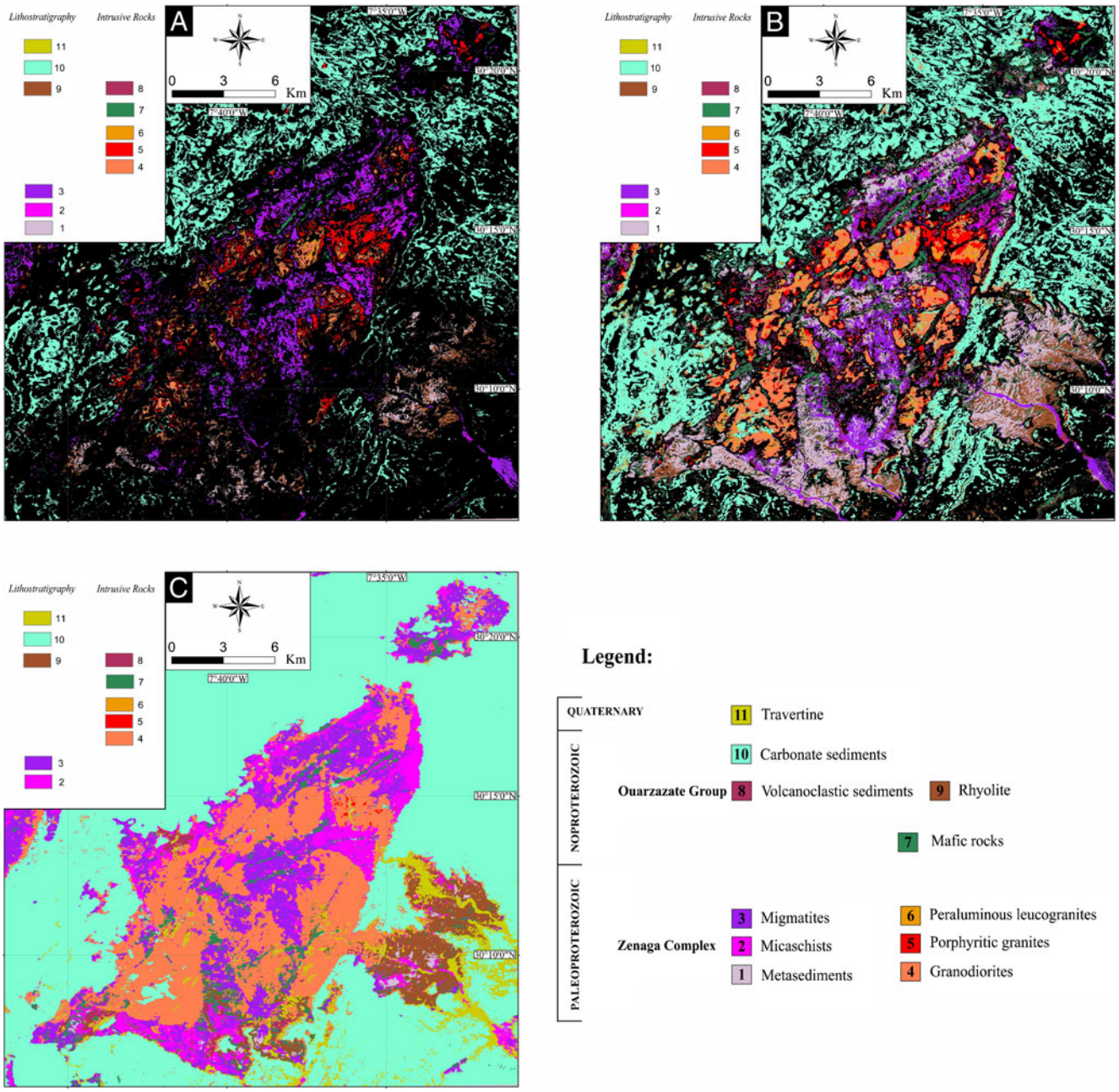


**Fig. 6** Output classification with color indicating the closest matches in the spectral similarity and derived from classification algorithms using: **a** spectral angle mapper algorithm; **b** spectral information divergence algorithm; and **c** maximum likelihood algorithm

one plutonic suite. Both SAM and SID are also very useful for discriminating metasedimentary rocks. SAM and SID provide excellent mapping tools to define spectra similarity of image by computing the angle between test reflectance spectrum and reference reflectance spectrum.

MLC algorithms effectively discriminate Proterozoic basement structures and contacts between metamorphic rocks, granitoid bodies, and carbonate cover surrounding the inlier. MLC algorithm improves rock discrimination in the basement of this area, demonstrating the existence of a number of metamorphic units and granitoid bodies that were not discriminated previously in field mapping (Faure-Muret et al. 1992).

Based on MLC algorithm interpretation, the Paleoproterozoic Zenaga metamorphic complex rocks are subdivided into three units corresponding to: (a) supracrustal metasediments; (b) micaschists; and (c) migmatites. MLC algorithm reveals the most informative training targets in high spectral data set and, with SID, can add more accuracy of distribution and the extent of metamorphic units. For example, the metasediments and

**Table 2** Confusion matrix and classification accuracies of the object oriented supervised classification

| (a) Contingency matrix of classification algorithm (SAM), applied to the training lithological classes | | | | | | | | | | | | |
|---|---|---|---|---|---|---|---|---|---|---|---|---|
| Classes | 1 | 2 | 3 | 4 | 5 | 6 | 7 | 8 | 9 | 10 | 11 | Total (%) |
| Unclassified | 12.50 | 60.34 | 78.40 | 38.99 | 69.33 | 69.06 | 24.38 | 94.63 | 96.13 | 64.51 | 100.00 | 64.88 |
| 1 | 87.50 | 0.47 | 0.00 | 0.00 | 0.00 | 0.00 | 0.00 | 0.00 | 0.00 | 0.00 | 0.00 | 2.82 |
| 2 | 0.00 | 27.68 | 0.00 | 0.00 | 0.67 | 0.00 | 0.00 | 0.00 | 0.00 | 0.00 | 0.00 | 5.02 |
| 3 | 0.00 | 0.00 | 21.60 | 0.00 | 0.00 | 0.00 | 0.00 | 0.00 | 0.00 | 0.00 | 0.00 | 0.75 |
| 4 | 0.00 | 0.00 | 0.00 | 49.54 | 0.00 | 11.75 | 0.00 | 0.00 | 0.00 | 0.00 | 0.00 | 4.38 |
| 5 | 0.00 | 11.51 | 0.00 | 0.00 | 30.00 | 0.00 | 0.00 | 0.00 | 0.00 | 0.00 | 0.00 | 4.57 |
| 6 | 0.00 | 0.00 | 0.00 | 11.47 | 0.00 | 19.18 | 0.00 | 0.00 | 0.00 | 0.00 | 0.00 | 2.93 |
| 7 | 0.00 | 0.00 | 0.00 | 0.00 | 0.00 | 0.00 | 49.38 | 0.00 | 0.00 | 0.00 | 0.00 | 4.41 |
| 8 | 0.00 | 0.00 | 0.00 | 0.00 | 0.00 | 0.00 | 0.00 | 5.37 | 0.00 | 0.00 | 0.00 | 0.22 |
| 9 | 0.00 | 0.00 | 0.00 | 0.00 | 0.00 | 0.00 | 26.25 | 0.00 | 3.87 | 0.00 | 0.00 | 2.51 |
| 10 | 0.00 | 0.00 | 0.00 | 0.00 | 0.00 | 0.00 | 0.00 | 0.00 | 0.00 | 35.49 | 0.00 | 7.50 |
| 11 | 0.00 | 0.00 | 0.00 | 0.00 | 0.00 | 0.00 | 0.00 | 0.00 | 0.00 | 0.00 | 0.00 | 0.00 |
| Total (%) | 100.00 | 100.00 | 100.00 | 100.00 | 100.00 | 100.00 | 100.00 | 100.00 | 100.00 | 100.00 | 100.00 | 100.00 |
| (b) Contingency matrix of classification algorithm (SID), applied to the training lithological classes | | | | | | | | | | | | |
| Unclassified | 7.14 | 7.00 | 68.00 | 24.77 | 1.00 | 42.21 | 0.00 | 41.61 | 18.71 | 21.37 | 85.82 | 26.69 |
| 1 | 91.07 | 11.98 | 0.00 | 0.00 | 23.33 | 0.48 | 0.00 | 0.00 | 0.00 | 0.00 | 0.00 | 7.00 |
| 2 | 0.89 | 57.54 | 0.00 | 1.38 | 41.33 | 0.00 | 0.00 | 0.00 | 0.00 | 0.53 | 0.00 | 14.00 |
| 3 | 0.00 | 0.00 | 32.00 | 2.75 | 0.00 | 0.00 | 0.00 | 1.34 | 16.77 | 0.00 | 1.80 | 2.26 |
| 4 | 0.00 | 0.00 | 0.00 | 52.75 | 0.00 | 9.11 | 0.00 | 0.67 | 0.00 | 0.00 | 1.80 | 4.49 |
| 5 | 0.89 | 19.28 | 0.00 | 0.00 | 28.67 | 0.00 | 0.00 | 0.00 | 0.00 | 0.00 | 0.00 | 5.89 |
| 6 | 0.00 | 0.00 | 0.00 | 8.72 | 0.00 | 28.06 | 0.00 | 6.04 | 0.00 | 0.00 | 0.00 | 4.04 |
| 7 | 0.00 | 0.00 | 0.00 | 4.59 | 0.00 | 8.87 | 88.44 | 0.00 | 24.52 | 0.00 | 0.77 | 10.35 |
| 8 | 0.00 | 0.00 | 0.00 | 1.83 | 0.00 | 8.39 | 0.00 | 50.34 | 0.00 | 0.00 | 0.00 | 3.18 |
| 9 | 0.00 | 0.00 | 0.00 | 0.92 | 0.00 | 1.44 | 11.56 | 0.00 | 40.00 | 0.00 | 0.00 | 2.98 |
| 10 | 0.00 | 4.20 | 0.00 | 2.29 | 5.67 | 1.44 | 0.00 | 0.00 | 0.00 | 78.10 | 0.00 | 18.05 |
| 11 | 0.00 | 0.00 | 0.00 | 0.00 | 0.00 | 0.00 | 0.00 | 0.00 | 0.00 | 0.00 | 9.79 | 1.06 |
| Total (%) | 100.00 | 100.00 | 100.00 | 100.00 | 100.00 | 100.00 | 100.00 | 100.00 | 100.00 | 100.00 | 100.00 | 100.00 |
| (b) Contingency matrix of classification algorithm (MLC), applied to the training lithological classes | | | | | | | | | | | | |
| Unclassified | 0.00 | 0.00 | 0.00 | 0.00 | 0.00 | 0.00 | 0.00 | 0.00 | 0.00 | 0.00 | 0.00 | 0.00 |
| 1 | 100.00 | 0.00 | 0.00 | 0.00 | 0.00 | 0.00 | 0.00 | 0.00 | 0.00 | 0.00 | 0.00 | 3.12 |
| 2 | 0.00 | 99.69 | 0.00 | 0.00 | 1.33 | 0.00 | 0.00 | 0.00 | 0.00 | 0.00 | 0.00 | 17.99 |
| 3 | 0.00 | 0.00 | 99.20 | 0.00 | 0.00 | 0.00 | 0.00 | 0.00 | 0.00 | 0.00 | 0.00 | 3.46 |
| 4 | 0.00 | 0.00 | 0.00 | 100.00 | 0.00 | 0.00 | 0.00 | 0.00 | 0.00 | 0.00 | 0.00 | 6.08 |
| 5 | 0.00 | 0.31 | 0.00 | 0.00 | 98.67 | 0.00 | 0.00 | 0.00 | 0.00 | 0.00 | 0.00 | 8.31 |
| 6 | 0.00 | 0.00 | 0.00 | 0.00 | 0.00 | 100.00 | 0.00 | 0.00 | 0.00 | 0.00 | 0.00 | 11.63 |
| 7 | 0.00 | 0.00 | 0.00 | 0.00 | 0.00 | 0.00 | 100.00 | 0.00 | 0.00 | 0.00 | 0.00 | 8.93 |
| 8 | 0.00 | 0.00 | 0.00 | 0.00 | 0.00 | 0.00 | 0.00 | 100.00 | 0.00 | 0.00 | 0.00 | 4.16 |
| 9 | 0.00 | 0.00 | 0.80 | 0.00 | 0.00 | 0.00 | 0.00 | 0.00 | 100.00 | 0.00 | 0.00 | 4.35 |
| 10 | 0.00 | 0.00 | 0.00 | 0.00 | 0.00 | 0.00 | 0.00 | 0.00 | 0.00 | 100.00 | 0.00 | 21.14 |
| 11 | 0.00 | 0.00 | 0.00 | 0.00 | 0.00 | 0.00 | 0.00 | 0.00 | 0.00 | 0.00 | 100.00 | 10.82 |
| Total (%) | 100.00 | 100.00 | 100.00 | 100.00 | 100.00 | 100.00 | 100.00 | 100.00 | 100.00 | 100.00 | 100.00 | 100.00 |

micaschists are clearly distinguished in the eastern Tinoussem and Aguinane Valleys (Fig. 6b) using MLC analysis (Fig. 6c); however, in the field they, have been collectively mapped as Neoproterozoic volcanoclastic sediments.

Additionally, the mafic dykes that range in age from Paleoproterozoic to Mesozoic are distributed in numerous interlinked networks crosscutting the Proterozoic basement in varied directions. The mafic dykes are clearly visible on the images although discrimination of age and origin relations is not possible from the digital classification processing. Also, the Lower Ediacaran Ouarzazate Group and contacts with crystalline basement are clearly visible in the synthetic map (Fig. 6). The Lower Ediacaran Ouarzazate Group unconformably overlies the crystalline basement and consists of volcanoclastic formations outcropping along the borders of the inlier. Further west in the Taïfast depression, the Ouarzazate Group is composed of massive rhyolite (Faure-Muret et al. 1992; Admou et al. 2013). Surrounding the inlier, the Upper Ediacaran–Lowermost Cambrian Adoudou Group carbonates are easily distinguished from the underlying Proterozoic rocks and are covered by the Lower Cambrian carbonates at the northwest and south parts of the area.

The synthetic lithologic classification results are derived from transformation of the numerical image data into descriptive classes that categorize different geological outcrops. By virtue of digital image processing, we have transformed the raw data into an improved classification form that has more informational value. A large reduction in data quantity occurred during systematic preprocessing achievement and also during processing and classification.

The extracted synthetic maps (Fig. 6) employ the most useful spectral components defined in the images, based on optimized techniques that provide a reasonable segregation to predefined outcrops in the Iguerda inlier. Combining elements of the synthetic map (Fig. 6), recent ground truth geologic mapping, and the previously existing geologic map (Fig. 2), we have

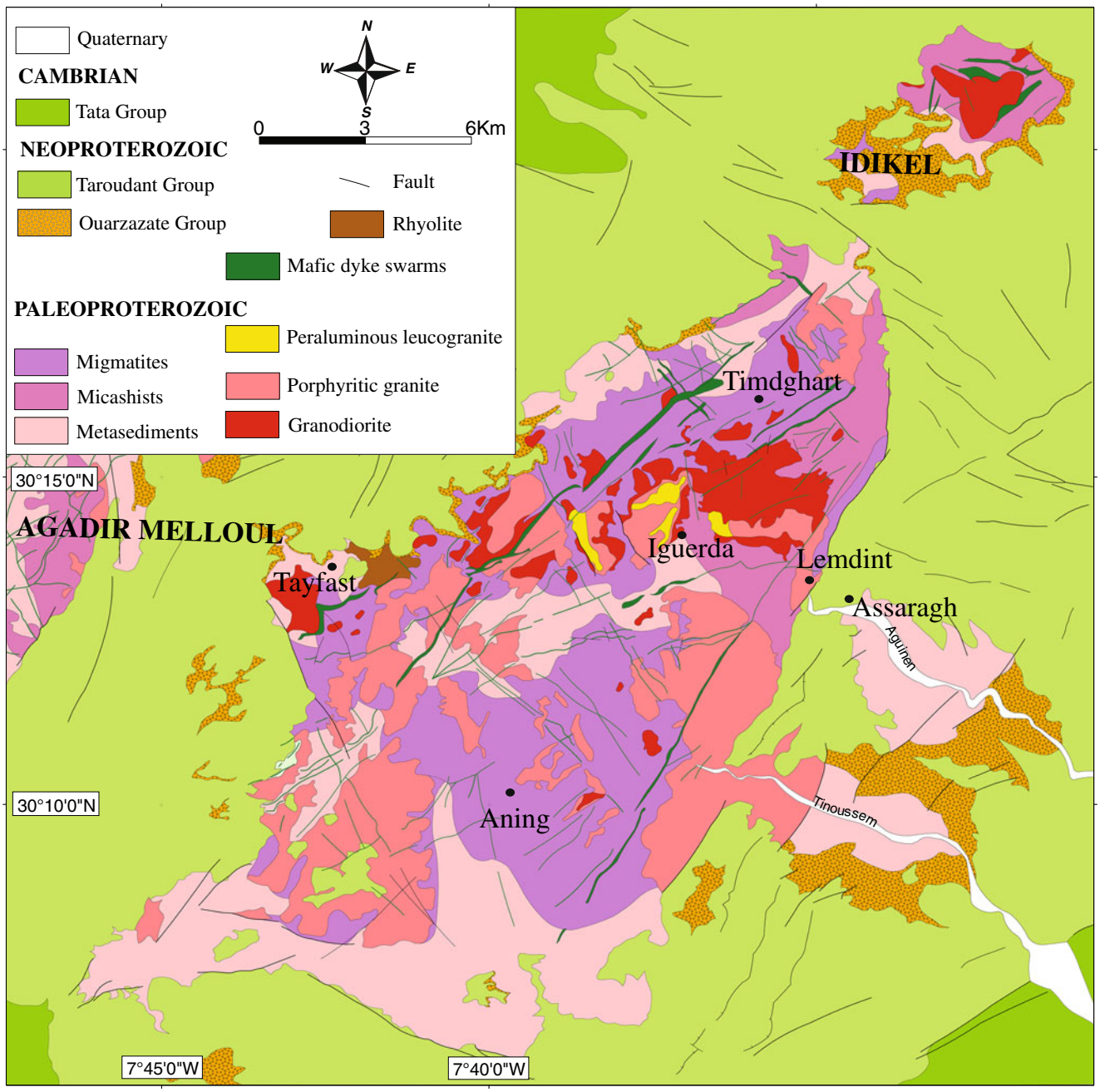


**Fig. 7** Geological map of the Iguerda area resulting from remote sensing interpretation of ASTER data

developed a new and improved geologic map combining these data (Fig. 7).

To sum up, the geologic remote sensing is based on statistical distribution assumptions included in ASTER imagery, image processing employed, and the inherent geologic character of the earth surface studied. As such, we do not claim that one classifier algorithm is better than another; algorithm performance is largely dependent on data type and the geologic region under investigation. However, in this specific study, our ability to discriminate lithological classes has been greatly facilitated through the use of SID, SAM, and MLC. At this point, this entire classifier algorithm set has been tested in this study through ground truth mapping in the Iguerda inlier. Ground truth mapping supports the remote sensing analysis whereby we are now able to discriminate basement rocks that hitherto were considered one unit. Improved rock discrimination is clearly evident in comparing earlier geologic maps of the Iguerda inlier (Fig. 2) with the digitally enhanced geologic map generated in this study (Fig. 7). Ultimately, the use of appropriate algorithms has greatly enhanced geological mapping in this arid area.

## Conclusions

The ASTER visualization is strategically designed to complement the objectives of structural study and geological mapping of the Iguerda inlier. Each algorithm used in this study can distinguish a limited number of lithological classes derived from the Iguerda inlier basement. The SID algorithm is most effective in distinguishing the majority of geological data. SAM and MLC algorithms also provide useful results, which can enhance the geological map agreement with the Agadir Melloul sheet, scale 1/100,000 with lithological evident classification. These algorithms improve rock discrimination in the metamorphic basement of this area, demonstrating the existence of a number of granitoid bodies and metamorphic units that were not discriminated previously in field mapping (Faure-Muret et al. 1992). Based on digital data algorithm interpretation, the Paleoproterozoic Zenaga metamorphic complex rocks are subdivided into three units corresponding to: (a) supracrustal metasediments; (b) micaschists; and (c) migmatites. Intrusive granitoids, which are subdivided into three categories ground truthed by our field observations, correspond to: (a) porphyritic granites; (b) granodiorites; and (c) peraluminous leucogranites. Given that ASTER data are sufficiently sensitive to detect differences in mineral associations in our study area, a porphyritic granite suite, granodiorite suite, and peraluminous leucogranites have been effectively discriminated.

In this study, the potential accuracy mapping of ASTER data has been tested on Iguerda Proterozoic outcrop discrimination, and the main results are illustrated in the new, digitally improved geologic map (Fig. 7) and summarized below:

1. Digital remote sensing enhances the geologic field mapping and laboratory analysis and helps in the petrographic and geochemical rock characterization and classification. These benefits are most pronounced in the discrimination of granitoid plutons. MLC algorithms effectively discriminate Proterozoic basement structures and contacts between metamorphic rocks, granitoid bodies, and carbonate cover surrounding the inlier. This algorithm improves rock discrimination in the metamorphic basement of this area, demonstrating the existence of a number of granitoid bodies and metamorphic units that were not discriminated previously in field mapping (Faure-Muret et al. 1992).
2. SAM and SID are useful for discriminating granitoids based on differences in silica content. These options provide excellent mapping tools to define spectra similarity of image by computing the angle between test reflectance spectrum and reference reflectance spectrum. Given that ASTER data are sufficiently sensitive to detect differences in mineral associations in our study area, a porphyritic granite suite, granodiorite suite, and peraluminous leucogranites have been effectively discriminated. MLC algorithm reveals the most informative training targets in high spectral data set and, with SID, can add more accuracy of distribution of plutonic bodies and the extent of metamorphic units.
3. Coupled with field observations and petrographic analyses, the remote sensing approaches applied in this study clearly demonstrate that hyperspectral analysis of ASTER data provides detailed lithologic discrimination that enhances significantly field mapping of metamorphic basement, such as the arid regions of the Anti-Atlas Mountains of Morocco.
4. In the case study of the Iguerda area, hyperspectral analyses of ASTER data allow to easily distinguish between the Precambrian basement and the overlying Ediacaran–Lowermost Cambrian cover. This application is especially useful for determining the main geological features of the Proterozoic basement, both between the different intrusive granitoids facies and diverse lithological units of the surrounding metamorphic rocks, as well as the crosscutting dyke swarms.

**Acknowledgments** This research was completed at GEOHYD Laboratory of the Cadi Ayyad University of Marrakech. Logistical support was provided by the geological mapping project of Agadir Melloul 19/2008, part of the National Program of Geological Mapping (PNCG) launched by the Ministère de l'Energie et des Mines du Maroc. Constructive reviews by two anonymous reviewers and editorial comments by François Roure substantially improved the presentation of the manuscript. We also thank André Michard whose suggestions helped improve the earlier version of the manuscript.

## References

Aboelkhair H, Ninomiya Y, Watanabe Y, Sato I (2010) Processing and interpretation of ASTER TIR data for mapping of rare-metal-enriched albite granitoids in the Central Eastern Desert of Egypt. J Afr Earth Sci 58(1):141–151. doi:10.1016/j.jafrearsci.2010.01.007

Abrams M (2000) The Advanced Spaceborne Thermal Emission and Reflection Radiometer (ASTER): data products for the high spatial resolution imagery on NASA's Terra platform. Int J Remote Sens 21:847–859. doi:10.1080/014311600210326

Admou H, Juteau T (1998) Discovery of a fossil oceanic hydrothermal system in the Late Precambrian Khzama ophiolite (Siroua massif, Anti-Atlas). Comptes Rendus de l'Académie des Sciences 327:335–340

Admou H, Hafid A, Soulaimani A, Simon B, Blein O, Ouanaimi H, Baudin T, El Janati M, Abia EH, Bouabdelli M (2013) Carte géologique du Maroc, feuille d'Assaragh 1/50 000. Notes et Mémoires Serv. Géol. Maroc 550 (in press)

Agard J (1954) Géologie et minéralisations de la boutonnière précambrienne d'Iguerda-Taïfast. Notes Serv Géol Maroc 120:57–89

Aït Malek H, Gasquet D, Bertrand JM, Letterier J (1998) Géochronologie U-Pb sur Zircorn de granitoides éburnéens et Panafricains dans la boutonnière protérozoïque d'Ighrem, Kerdous et Bas Draa (Anti Atlas Occidental, Maroc). CR Acad Sc Paris 327:819–826

Baltsavia EP (2002) Special section on image spectroscopy and hyper-spectral imaging. ISPRS J Photogramm Remote Sens 57:169–170

Ben-Dor E, Kruse FA (1994) The relationship between the size of spatial subsets of GER 63 channel scanner data and the quality of the Internal Average Relative Reflectance (IARR) correction technique. Int J Remote Sens 15(3):683–690

Bilal E, Derre C (1989) Les granitoides protérozoïques calco-alcalins de la boutonnière d'Iguerda-Tayfst (Anti Atlas, Maroc). Notes et Mémoires Serv Géol Maroc 83:5–25

Boardman JW, Kruse FA, Green RO (1995) Mapping target signatures via partial unmixing of AVIRIS data. Summaries of the 5nd Annual JPL Airborne Geoscience Workshop. JPL Publ 1:23–26

Bouougri EA, Porada H (2002) Mat-related sedimentary structures in Neoproterozoic peritidal passive margin deposits of the West African Craton (Anti-Atlas, Morocco). Sediment Geol 153(3–4):85–106

Burkhard M, Caritg S, Helg U, Robert-charrue C, Soulaimani A (2006) Tectonics of the Anti-Atlas of Morocco. C R Geosci 338:11–24. doi:10.1016/j.crte.2005.11.012

Caritg S, Burkhard M, Ducommun R, Helg U, Kopp L, Sue C (2004) Fold interference patterns in the Late Palaeozoic Anti-Atlas belt of Morocco. Terra Nova 16:27–37. doi:10.1111/j.1365-3121.2003.00525.x

Chabrillat S, Goetz AFH, Olsen HW, Krosley L, Noe DC (2000) The search for swelling clays along the Colorado Front Range: results from field spectrometry and hyperspectral imagery. JPL Publ 21:2363–2388

Chen CT, Landgrebe DA (1989) A spectral feature design system for the HIRIS/MODIS era. IEEE Trans Geosci Remote Sens 27:681–686

Chèvremont Ph, Blein O, Razin Ph, Simon B, Baudin T, Ouanaimi H, Soulaimani A, El Janati M, Bouabdelli M, Abia EH, Admou H, Hafid A, Beni Akhy R (2013) Notice explicative carte géol. Maroc (1/50 000), feuille d'Ighriy, Notes et Mémoires Serv. Géol. Maroc, N° 548 bis (in press)

Choubert G (1943) Sur le Géorgien de l'Anti-Atlas. C R Acad Sci Paris 216:69–70

Choubert G (1947) L'accident majeur de l'Anti-Atlas. C R Acad Sci Paris 224:1172–1173

Choubert G (1963) Histoire géologique du Précambrien de l'Anti-Atlas. Notes Mém. Serv. Géol. Maroc 162, p 352

D'Lemos RS, Inglis JD, Samson SD (2006) A newly discovered orogenic event in Morocco: Neoproterozic ages for supposed Eburnean basement of the Bou Azzer inlier, Anti-Atlas Mountains. Precambrian Res 147:65–78. doi:10.1016/j.precamres.2006.02.003

De Carvalho OA, Meneses PR (2000) Spectral correlation mapper (SCM): an improvement on the spectral angle mapper (SAM). JPL Publ 9(00–18):1–9

El Aouli EH, Ikenne M, Gasquet D (2001) Affinités géochimiques et implications géodynamiques des dykes basiques de la boutonnière d'Iguerda-Taïfast (Anti-Atlas, Maroc). Géologie Méditerranéenne XXVIII:193–202

El Aouli EH, Ikenne M, Beraaouz EH, Mortaji A (2004) Les roches basiques des boutonnières d'Agadir Melloul et d'Iguerda-Taïfast: témoins de l'histoire préorogénique de la chaîne panafricaine de l'Anti-Atlas (Maroc). Estudios Geologicos 60:11–20

El Aouli EH, Ikenne M, Amaouain H (2010) Petrographic and geochemical characterization of cryogenian mafic dykes of the Iguerda-Taïfast inlier (Central AntiAtlas, Morocco). Int J Geomatics Geosci 3:355–371

El Bahat A, Ikenne M, Söderlund U, Cousens B, Youbi N, Ernst R, Soulaimani A, El Janati M, Hafid A (2013) U-Pb baddeleyite ages and geochemistry of dolerite dykes in the Bas Drâa Inlier of the Anti-Atlas of Morocco: newly identified 1380 Ma event in the West African Craton. Lithos. doi: 10.1016/j.lithos.2012.07.022

El Hadi H, Simancas JF, Martinez-Poyatos D, Azork A, Tahiri A, Montero P, Fanning CM, Bea F, Gonzalez-Lodeiro F (2010) Structural and geochronological constraints on the evolution of the Bou Azzer Neoproterozoic ophiolite (Anti-Atlas, Morocco). Precambrian Res 182:1–14. doi:10.1016/j.precamres.2010.06.011

Faure-Muret A, Choubert G, Dahmani M, El Mouatani A, Horrenberger JC, Salem M (1992) Carte géologique du Maroc à 1/100 000–feuille Agadir Melloul. Notes et Mém. Serv. Géol, Maroc, 359

Gasquet D, Chèvremont P, Baudin T, Chalot-Prat F, Guerrot C, Cocherie A, Roger J, Hassenforder B, Cheilletz A (2004) Polycyclic magmatism in the Tagragra d'Akka and Kerdous-Tafeltast inliers (Western Anti-Atlas, Morocco). J Afr Earth Sci 39:267–275. doi:10.1016/j.jafrearsci.2004.07.062

Gasquet D, Levresse G, Cheilletz A, Azizi-Samir MR, Mouttaqi A (2005) Contribution to a geodynamic reconstruction of the Anti-Atlas (Morocco) during Pan-African times with the emphasis on inversion tectonics and metallogenic activity at the Precambrian-Cambrian transition. Precambrian Res 140:157–182. doi:10.1016/j.precamres.2005.06.009

Gasquet D, Ennih N, Liègeois JP, Soulaimani A, Michard A (2008) The pan-african belt of morocco, in: Continental evolution: the geology of morocco. In: Michard A, Saddiqi O, Chalouan A, Frizon D (eds) Structure, stratigraphy, and tectonics of the africa-atlantic-mediterranean triple junction, de Lamotte Springer Verl., vol 116. Berlin, Heidelberg, p 404. doi:10.1007/978-3-540-77076-3

Green AA, Berman M, Switzer P, Craig MD (1988) A transformation for ordering multispectral data in terms of image quality with implications for noise removal. IEEE Trans Geosci Remote Sens 26(1):65–74. doi:10.1109/36.3001

Hafid A, Sagon JP, Fonteilles M, Moutte J (1998) Existence de deux séries tholéïtiques distinctes parmi les dolérites du Protérozoïque supérieur de la boutonnière d'Irherm; (Anti-Atlas Occidental, Maroc). C R de l'Acad Sci 326:21–26

Hafid A, Sagon JP, Saquaque A, El Boukhari A, Saidi A (1999) Pétrologie et contexte géodynamique du magmatisme basique néoproterozoïque de la boutonnière d'Iguerda-Taïfast (Anti-Atlas central, Maroc). Afr Geosci Rev 6(2):121–133

Hafid A, Blein O, Admou H, Soulaimani A, Razin P, Simon B, Ouanaimi H, El Janati M, Chèvremont P, Baudin T, Bouabdelli M, Abia EH (2013) Notice de la carte géologique du Maroc. Feuille d'Assaragh 1/50 000. Notes et Mémoires Serv. Géol. Maroc 550 bis (in press)

Hassenforder B (1987) La tectonique panafricaine et varsique de l'Anti Atlas dans le massif de Kerdous (Maroc): Thèse d'Etat. Université de Strasbourg, France

Hefferan KP, Karson JA, Saquaque A (1992) Proterozoic collisional basins in a Pan-African suture zone, Anti-Atlas Mountains Morocco. Precambrian Res 54(2–4):295–319

Hefferan KP, Admou H, Karson JA, Saquaque A (2000) Anti-Atlas (Morocco) role in Neoproterozoic Western Gondwana reconstruction. Precambrian Res 103:89–96

Henderson TL, Baumgardner MF, Franzmeier DP, Stott DE, Coster DC (1992) High dimensional reflectance analysis of soil organic matter. Soil Sci Soc Amer 56:865–872

Hunt GR (1979) Near infrared (1.3–2.4 lm) spectra of alteration minerals—potential for use in remote sensing. Geophysics 44(12):1974–1986

Inglis JD, D'Lemos RS, Samson SD, Admou H (2005) Geochronological constraints on Late Precambrian intrusion, metamorphism, and tectonism in the Anti-Atlas Mountains. J Geol 113:439–450

Jia X, Richards A (1994) Efficient maximum likelihood classification for imaging spectrometer data sets. IEEE Trans Geosci Remote Sens 32(2):274–281. doi:10.1109/36.295042

Knipling EB (1970) Physical and physiological basis for the reflectance of visible and near-infrared radiation from vegetation. Remote Sens Environ 1:155–159

Kouyaté D, Söderlund U, Youbi N, Ernst R, Hafid A, Ikenne M, Soulaimani A, Bertrand H, El Janati M, Chaham KR (2013) U-Pb baddeleyite ages of 2040 Ma, 1650 Ma and 885 Ma on dolerites in the West African Craton (Anti-Atlas inliers): possible links to break-ups of Precambrian supercontinents. Lithos. doi:10.1016/j.lithos.2012.04.028

Kruse FA (1988) Use of Airborne Imaging Spectrometer data to map minerals associated with hydrothermally altered rocks in the northern Grapevine Mountains, Nevada and California. Remote Sens Environ 24(1):31–51

Kruse FA, Boardman JW, Lefkoff AB, Heidebrecht KB, Shapiro AT, Barloon PJ, Goetz AFH (1993) The spectral image processing system (SIPS)—interactive visualization and analysis of imaging spectrometer data. Remote Sens Environ 44:145–163

Lang HR (1999) Chapter 7, Stratigraphy. In: Renz AN (ed) Remote sensing for the earth sciences, manual of remote sensing, New York, NY, John Wiley and Sons 3:351–368

Leblanc M (1976) The Proterozoic oceanic crust at Bou-Azer. Nature 261:34–35

Leblanc M, Moussine-Pouchkine A (1994) Sedimentary and volcanic evolution of a Neoproterozoic continental margin (Bleïda, Anti-Atlas, Morocco). Precambrian Res 70:25–44

Liu JG, Mason PJ (2009) Essential image processing and GIS for remote sensing. Wiley-Blackwell, New York, p 450

Marsh SE, McKeon JB (1983) Integrated analysis of high-resolution field and airborne spectroradiometer data for alteration mapping. Econ Geol 78(4):618–632

Massironi M, Bertoldi L, Calafa P, Visonà D, Bistacchi A, Giardino C, Schiavo A (2008) Interpretation and processing of ASTER data for geological mapping and granitoids detection in the Saghro massif (eastern Anti-Atlas, Morocco). Geosphere 4:736–759. doi:10.1130/GES00161.1

McPherson AA, Halls LS (2007) Development of the Australian National Regolith Site Classification Map. Geoscience Australia, p 37

Michard A, Soulaimani A, Hoepffner C, Ouanaimi H, Baidder L, Rjimati EC, Saddiqi O (2010) The south-western branch of the Variscan Belt: evidence from Morocco. Tectonophysics 492:1–24. doi:10.1016/j.tecto.2010.05.021

Mortaji A, Ikenne M, Gasquet D, Barbey P, Stussi JM (2000) Les granitoïdes paléoprotérozoïques des boutonnières du Bas Draa et de la Tagragra d'Akka (Anti-Atlas occidental, Maroc); un élément du puzzle géodynamique du craton ouest-Africain. J Afr Earth Sci 31:523–538

North American Stratigraphic Code (2005) Am Assoc Pet Geol Bull 69:1547–1591

O'Connor EA (2010) Geology of the Draa, Kerdous, and Boumalne Districts, Anti-Atlas, Morocco. Technical Report IR/10/072, British Geol. Surv., Keyworth, Nottingham, England, 310 p

Ouanaimi H, Chèvremont P, Blein O, Simon B, Baudin T, Razin P, Soulaimani A, Abia EH, Admou H, Hafid A, El Janati M, Bouabdelli M (2003) Carte géologique du Maroc, feuille d'Ighriy 1/50 000: Notes et Mémoires Serv. Géol. Maroc 548 (in press)

Piqué A, Bouabdelli M, Soulaimani A, Youbi N, Iliani M (1999) Les conglomérats du PIII (Néoprotérozoïque supérieur) de l'Anti Atlas (Sud du Maroc): molasses panafricaines, ou marqueurs d'un rifting fini-protérozoïque? C R Acad Sci 328:409–414, Paris

Raines GL, McGee LC, Sutley SJ (1985) Near-infrared spectra of West Shasta gossans compared with true and false gossans from Australia and Saudi Arabia. Econ Geol 80:2230–2239

Richards JA (1993) Remote sensing digital image analysis: an introduction, 2nd edn. Springer, Berlin

Richards JA, Jia X (2006) Remote sensing digital image analysis. Springer, Berlin

Rocci G, Bronner G, Deschamps M (1991) Crystalline basement of the West African Craton. In: Dallmeyer RD, Lécroché JP (eds). Springer-Verlag, Berlin, pp 31–61

Roger J, Chèvremont P, Razin P, Thiéblemont D, Baudin T, Calvès G, Aznar-Conseil (2006) Notice explicative de la carte géologique du Maroc (1/50 000). Feuille Tlatat Ida Gougmar. Notes et Mémoires du Service Géologique du Maroc 498 bis

Rogge DM, Rivard B, Zhang J, Sanchez A, Harris J, Feng J (2007) Integration of spatial–spectral information for the improved extraction of endmembers. Remote Sens Environ 110(3):287–303. doi:10.1016/j.rse.2007.02.019

Rowan LC, Goetz AFH, Ashley RP (1977) Discrimination of hydrothermal altered rocks in visible and near infrared multispectral images. Geophysics 42:512–535

Rowan LC, Salisbury JW, Kingston MJ, Vergo NS, Bostick NH (1991) Evaluation of visible, near-infrared and thermal-infrared reflectance spectra for studing thermal alteration of Pierre shale, Wolcott, Colorado. Geophys Res 96(18):18047–18057

Rowan LC, Schmidt RG, Marsa JC (2011) Distribution of hydrothermally altered rocks in the RekoDiq, Pakistan mineralized area based on spectral analysis of ASTER data. Remote Sens Environ 101:74–87

Ruiz G, Sebti S, Saddiqi O, Negro F, Frizon de Lamotte D, Stockli D, Foeken J, Stuart F, Barbarand J (2011) Mesozoic to recent denudation patterns in the Anti-Atlas of SW Morocco. Terra Nova 23:35–41. doi:10.1111/j.1365-3121.2010.00980.x

Saquaque A, Admou H, Cisse A, Benyoussef A, Reuber I (1989) Les intrusions calco-alcalines de la boutonnière de Bou Azzer-El Graara (Anti-Atlas): marqueurs de la déformation panafricaine majeure dans un contexte de collision d'arc. C R Acad Sci Paris 308:1279–1283

Schowengerdt RA (2007) Remote sensing: models and methods for image processing. Elsevier, Amsterdam

Soulaimani A (1998) Interactions socle/couverture dans l'Anti-Atlas occidental (Maroc): Rifting du Protérozoïque terminal et Orogenèse hercynienne, Thèse d'Etat, 3 Juillet 1998, Univ. Cadi Ayyad, Marrakech

Soulaimani A, Burkhard M (2008) The Anti-Atlas chain (Morocco): the southern margin of the Variscan belt along the edge of the West African Craton. In: Ennih N, Liégeois JP (eds) The boundaries of the West African Craton. Geological Society London, Special Publications 279:433–452. doi: 10.1144/SP297.20

Soulaimani A, Bouabdelli M, Piqué A (2003) L'extension continentale au Néoprotérozoïque supérieur-Cambrien inférieur dans l'Anti-Atlas (Maroc). Bull Soc Géol France 174:83–92

Thomas RJ, Chevallier LP, Gresse PG, Harmer RE, Eglington BM, Armstrong RA, de Beer CH, Martini JEJ, de Kock GS, Macey PH, Ingram BA (2002) Precambrian evolution of the Sirwa Window, Anti-Atlas Orogen, Morocco. Precambrian Res 118:1–57

Thomas RJ, Fekkak A, Ennih N, Errami E, Loughlin SC, Gresse PG, Chevallier LP, Liégeois JP (2004) A new lithostratigraphic framework for the Anti-Atlas Orogen, Morocco. J Afr Earth Sci 39(3–5):217–226

Townsend TE (1987) Discrimination of iron alteration minerals in visible and near infrared data. Geophys Res 92(B2):1441–1454

Walsh GJ, Aleinikoff JN, Benziane F, Yazidi A, Armstrong TR (2002) U-Pb zircon geochronology of the Paleoproterozoic Tagragra de Tata inlier and its Neoproterozoic cover, western Anti-Atlas, Morocco. Precambrian Res 117(1–2):1–20

Walsh GJ, Benziane F, Aleinikoff JN, Harrison RW, Yazidi A, Burton WC, Quick JE, Saadane A (2012) Neoproterozoic tectonic evolution of the Jebel Saghro and Bou Azzer-El Graara inliers, eastern

Xu Z, Zhao H (2008) A new spectral unmixing algorithm based on spectral information divergence. Proc SPIE 7127(7):712–726

Yamaguchi Y, Kahle AB, Tsu H, Kawakami T, Pniel M (1998) Overview of Advanced Spaceborne Thermal Emission and Reflection Radiometer (ASTER). IEEE Transactions on Geoscience and Remote Sensing 36-1062-1071

Youbi N, Martins LT, Munhá JM, Ibouh H, Madeira J, Aït Chayeb H, El Boukhari A (2003) The Late Triassic-Early Jurassic volcanism of Morocco and Portugal in the framework of the Central Atlantic Magmatic province. An overview. In: Hames WE, McHone JG, Renne PR Ruppel C (eds.) The Central Atlantic Magmatic Province: insights from fragments of Pangea. AGU Geophysical Monograph Series 136:179–207

Yuhas RH, Goetz AFH, Boardman JW (1992) Discrimination among semi-arid landscape endmembers using the spectral angle mapper (SAM) algorithm. JPL Publ 4(92–41):147–149